DOI: 10.1002/ ((please add manuscript number))

Article type: (**Full Paper**)

Ultrasensitive Exhaled Breath Sensors Based on Anti-Resonant Hollow Core Fiber with *in Situ* Grown ZnO-Bi_2O_3 Nanosheets

Wei Liu [a,b], Yu Zheng [b], Zhe Wang [b], Zhixun Wang [b], Jiao Yang [b], Mengxiao Chen [b], Miao Qi [b], Shafiq Ur Rehman [a], Perry Ping Shum [c], Ling Zhu [a]*& Lei Wei [b,d]*

a. Key Laboratory of Optoelectronic Device and Systems of Ministry of Education and Guangdong Province, College of Optoelectronic Engineering, Shenzhen University, Shenzhen, 518060, PR China

b. School of Electrical and Electronic Engineering, Nanyang Technological University, 50 Nanyang Avenue, Singapore, 639798, Singapore

c. Department of Electrical and Electronic Engineering, Southern University of Science and Technology, Shenzhen, 518055, PR China

d. CNRS/NTU/THALES, UMI3288, Research Techno Plaza, 50 Nanyang Drive, Singapore, 637553, Singapore

*Email address: zhuling@szu.edu.cn, wei.lei@ntu.edu.sg;

Keywords: Anti-resonant; In situ grown; Exhaled breath; Acetone; Gas sensors

Abstract

Combination of anti-resonant hollow-core fiber (HCF) and semiconductor nanomaterial is an effective strategy to obtain high-performance gas sensors with exceptional sensitivity and low power consumption. However, controlling the semiconductor morphology onto HCF is a major challenge to achieve the desired gas sensor with the enhanced sensitivity. Here, a ZnO-Bi_2O_3 nanosheets (NSs) heterostructure is grown *in situ* on the surface of HCF by sol-gel and hydrothermal methods. ZnO-Bi_2O_3 NSs serving as electron acceptors trap electrons after acetone adsorption and then change the refractive index of the surface of HCF. Benefiting from the unique sheet structure and the synergetic effects for multi-component, the resulting ZnO-Bi_2O_3 NSs enabled HCF gas sensor exhibits high sensitivity, selectivity and repeatability for detecting acetone at room temperature, particularly in the low concentration range, with the theoretical limit of detection down to 140 parts-per-billion (ppb). Meanwhile, the successful application of the ZnO-Bi_2O_3 NSs enabled HCF gas sensor to distinguish the exhaled breath from the healthy individuals and simulated diabetic cases is demonstrated, which paves the way to achieve non-invasive, ultra-sensitivity gas sensing at room temperature for the early diagnosis of diabetes.

Introduction

Abnormal content of gaseous volatile organic compounds (VOCs) in human exhaled breath can reflect various health conditions, such as high levels of acetone portend diabetes risk, abnormal formaldehyde levels predict breast cancer risk.[1-3] As a result, ultrasensitive detection of gas molecular is important for the application of breath diagnostics. Generally speaking, conventional gas sensors (typically semiconductor and optical gas sensors) encounter many downsides, including the fail low detection limit, high power consumption, and low sensitivity.[4-6] For example, although the semiconductor gas sensor has the advantages of high sensitivity, fast response time, and high chemical stability, the operation requires a high temperature, which normally causes high power consumption, overconsumption of energy, and even safety issues.[7-9] On the contrary, the optical fiber sensor offers an alternative platform to implement the VOCs sensors thanks to its several advantages of intrinsic safety, immunity to working temperature, chemical inertness, low detection limit, and seamless connection to the communication network.[10-12] In particular, the combination of semiconductor and optical fiber sensor has attracted wide and significant attention. Recently, various semiconductor materials have been reported to be coated on optical fiber to implement the VOCs gas sensors, and the sensing mechanism is based on the induced refractive index change caused by the reaction of semiconductor material and gas molecular.[13-18] Therefore, to improve the sensing performance, it is very important to control the growth of semiconductor materials on the optical fiber. However, the current methods mainly focus on dip-coating semiconductor materials on the optical fiber, which commonly damage the original morphology features and fail to maximize material utilization.

From the viewpoint of accessible materials, ZnO and Bi_2O_3 have the advantages of tunable electrical conductivity, high electron affinity, wide bandgap, and environmentally benign,[19-22] making them promising high-sensitive materials for constructing gas sensors. Furthermore, substantial experimental and theoretical efforts have been devoted to the exploration of a two-dimension nanosheet (NS) structure for gas sensors due to its large specific surface area, high electrical conductivity, and excellent flexibility, which can be one of the ideal structures employed in gas sensors.[23-27] Special emphasis is given to two-dimension wormhole-like inter-nanosheets, which can efficiently combine the merits of two-dimension nanosheets and

porous functional materials, working together to synergistically enhanced gas-sensing performance. Despite the great progress made, two-dimension nanosheets materials usually possess high working temperature in the application of semiconductor gas sensor, which is not very favorable for the detection of room temperature in human exhaled breath due to their unsatisfactory responses. It is thus quite imperative to further explore feasible strategies for the two-dimension nanosheets materials system integrated with optical fiber to achieve desirable gas sensing operated at room temperature.

In this work, we propose and demonstrate an ultrasensitive exhaled breath sensor based on the *in situ* growth of ZnO-Bi_2O_3 NSs on the side surface of an anti-resonant hollow-core fiber (HCF) by sol-gel and hydrothermal method. The resulting gas sensor exhibits an ultra-high sensitivity, excellent selectivity and repeatability for acetone sensing at room temperature. Moreover, the response and recovery times are successfully controlled within one minute, which can satisfy the requirement of the practical applications. In particular, the theoretical limit of detection is further down to 140 ppb, and the maximal acetone concentration range can reach 100 ppm, while the HCF gas sensor exhibits more enhanced gas sensing in the low concentration range. Also, theoretical simulation explains the mechanism of anti-resonance based on the change of the reflective index. As a proof of demonstration, the measurement of exhaled breath proves that the resulting HCF-based gas sensor can distinguish individuals with or without diabetes.

Results and Discussion

The sensing mechanism of the proposed HCF-based gas sensor can be explained intuitively by using the illustrations in Figure 1. The sensor is fabricated by splicing the lead-in and lead-out single-mode fibers (SMFs) with a section of HCF. Before the process of splicing, a facile *in situ* method is applied to grow ZnO-Bi_2O_3 NSs on the side surface of HCF to the formation of the gas detection layer, which can react with the target gas and modulate the refractive index. COMSOL Multiphysics software was used to simulate the mode field distribution of the ZnO-Bi_2O_3 NS coated HCF with a full-vector finite element method (FEM).[28] Figure 1a shows the mode field of anti-resonant wavelength (λ = 1540 nm), which is confined in the hollow core of the fiber as the guiding core mode. The mode field distributions of HCF without ZnO-Bi_2O_3 NSs

are shown in Figure S1a-d. Figure S1a-b indicate that the anti-resonant mode is mainly confined in the air core. Figure S1c-d illustrate that the resonant mode is leaked out of the air core and radiated into the cladding. The mode filed distributions of HCF with ZnO-Bi_2O_3 NSs are shown in Figure S1e-h, which indicates that the anti-resonant reflecting optical waveguide is still valid after the ZnO-Bi_2O_3 NSs are grown. However, when the ZnO-Bi_2O_3 NS was coated on the HCF, the inherent confine of the core mode was modulated in the fiber. This can be attributed to the refractive index of the core is less than that of silica, and the refractive index of silica is less than that of ZnO-Bi_2O_3 NS (Figure S1). Thus, the cladding of silica and ZnO-Bi_2O_3 NS are combined to form a double-layered Fabry-Pérot resonator. In this process, the guided light is reflected by the layer of ZnO-Bi_2O_3 NS and propagates in the core of HCF (Figure 1b), which is an anti-resonant condition, mismatching between the wavelengths and the resonant condition of the resonator.[18, 29] Therefore, the wavelength of the lossy dips (λ_r) at the anti-resonant condition can be expressed as the following formula:[30]

$$\lambda_r = \frac{2(d_0\sqrt{n_0^2 - n^2} + d_1\sqrt{n_1^2 - n^2})}{m}$$

where the d_0 and d_1 are the thickness of silica and the thickness of ZnO-Bi_2O_3 NS layer, respectively. n, n_0, and n_1 are the refractive index of the air, the silica and the layer of ZnO-Bi_2O_3 NS, respectively. m is the resonance order. When the layer of ZnO-Bi_2O_3 NS exposes to the target gas, the chemical reaction between the gas molecules and ZnO-Bi_2O_3 NS leads to a change in the refractive index of ZnO-Bi_2O_3 NS (Figure 1c). The refractive index of the Fabry-Pérot resonator is changed, and then the wavelength of the lossy dips corresponding to the resonant condition is shifted based on the above formula. Thus, the corresponding target gas signal can be detected by the shifts of the wavelength, and the use of such a double-layered Fabry-Pérot resonator makes ultrasensitive gas sensing possible.

The schematic of the *in situ* growth of ZnO-Bi_2O_3 NSs on optical fibers is depicted in Figure 2a. First, the HCF was employed as the sensing fiber with the fiber diameter of 125 μm, the core diameter of 50 μm, and the length of 3 cm, respectively. Then, the HCF was etched under hydrofluoric acid (HF) solution to remove the surface impurities and increase surface roughness. Next, the HCF was treated with ultraviolet ozone to increase the hydroxyl groups (-OH) on the surface, which can contribute the material formation on the HCF surface.[31] Afterward, the ZnO layer coating on the

surface of HCF was prepared using the sol-gel technique,[32] followed by an important growth step of ZnO thin film consist of many nanoparticles, where a pyrolytic transformation of PVP/$Zn(NO_3)_2$ into uniform ZnO thin film occurred on the surface of HCF after annealing at 300 °C for 2 h, as shown in Figure 2b and Figure S2, and eventually the growth of hierarchical Bi_2O_3 NSs on the HCF through hydrothermal treatment. To observe the morphological, field-emission scanning electron microscopy (FESEM) images reveal that a layer of ZnO-Bi_2O_3 NSs is uniformly grown on the surface of HCF (Figure 2c), and the enlarged image further proves this point in the insets. The thickness of ZnO-Bi_2O_3 NSs layer can be directly observed through the cross-section view (Figure 2d), which is 285 nm as shown in the insets. Magnified FESEM images reveal that the morphologies are composed of numerous thin interconnected nanosheets with the average thickness about 10 nm (Figure S3), forming wormhole-like inter-nanosheets and nanopores throughout the hierarchical structure (Figure 2e, f). Elemental mapping images of Zn, Bi and O indicate the successful decoration and homogeneous distribution of every component over the entire HCF (Figure 2g).

To further comprehend the detailed structure of as-fabricated ZnO-Bi_2O_3 NSs as shown in Figure 3a, the individual ZnO-Bi_2O_3 NS is revealed by transmission electron microscopy (TEM) images (Figure 3b, 3c). Further TEM analysis shows that the wrinkles-like structures provide a substantial number of active sites for target gas adsorption-desorption. The high-resolution TEM (HRTEM) image of the ZnO-Bi_2O_3 NS shows some visible lattice fringes (Figure 3d). The interplanar distance is confirmed to be 0.28 nm and 0.38 nm, which correspond to the (100) plane of hexagonal wurtzite ZnO and the (110) plane of cubic Bi_2O_3.[33-34] Meanwhile, the corresponding selected-area electron-diffraction (SAED) in Figure 3e is revealed that the polycrystalline nature of ZnO-Bi_2O_3 NS, which agrees well with the result of HRTEM, suggesting that the ZnO-Bi_2O_3 NSs possess likely a preferential exposed plant of (100) and (110) for ZnO and Bi_2O_3, respectively. It is worth noting that the X-ray diffraction (XRD) patterns of the synthesized ZnO-Bi_2O_3 NSs reveal that this sample contains the mixed phases of hexagonal wurtzite ZnO and cubic Bi_2O_3, which is in good agreement with the above analysis results (Figure S4). The energy dispersive X-ray (EDX) spectra demonstrate the homogeneous Zn, Bi, and O distribution throughout the entire nanosheets (Figure 3f and Figure S5), which indicate the successful fabrication of ZnO-Bi_2O_3

heterojunction during the process of hydrothermal treatment.

The X-ray photoelectron spectroscopy (XPS) survey reveals that ZnO-Bi_2O_3 NSs mainly comprise Zn, Bi and O elements (Figure 4a). The O 1s-related three peaks for ZnO thin film and ZnO-Bi_2O_3 NSs at 530.1, 530.9 and 532.0 eV correspond to crystal lattice oxygen (O_c), deficient oxygen (O_v) and adsorbed oxygen (O_{ads}) species or OH groups, respectively (Figure 4b).[35] Herein, the deficient oxygen ratios can be calculated to be 32.4% and 50.2% with the ratio of the integral area of the deficient oxygen peak to the whole area of the O 1s peak for the ZnO thin film and ZnO-Bi_2O_3 NSs, respectively. This can be attributed to the reason that the designed morphologies of ZnO-Bi_2O_3 NSs induce more oxygen vacancies in the sample. Specifically, the Zn 3p-related two peaks can be assigned to the Zn $3p_{3/2}$ and Zn $3p_{1/2}$ orbits (Figure 4c),[36] which observe all the Zn 3p peaks shift to the high binding energy for ZnO-Bi_2O_3 NSs compared to ZnO thin film. The result suggests that the Zn electron densities for ZnO-Bi_2O_3 NSs are slightly decreased relative to ZnO thin film, leading to higher binding energies. This is due to the larger electronegativities of Bi^{3+} (2.02) than Zn^{2+} (1.65), which can draw electrons from the Zn element.[37-38] Moreover, the Bi 4f-related two peaks can be assigned to the Bi $4f_{7/2}$ and Bi $4f_{5/2}$ orbits at 156.2 and 162.1 eV, respectively. The results indicate that the existence of ZnO and Bi_2O_3, and the Zn^{2+} state of Zn in ZnO and the Bi^{3+} state of Bi in Bi_2O_3. In addition, the Nyquist plot (Figure S6) of the electrochemical impedance shows that the charge transfers resistance value of ZnO thin film (4.32 Ω) is 3.87 times lower than the transfer resistance of ZnO-Bi_2O_3 NSs (16.74 Ω), demonstrating that the property of electron transfers is significantly enhanced by the grown of ZnO-Bi_2O_3 NSs.

It is highly urgent to develop non-invasive, sensitive and selective methods to detect the gas biomarkers associated with the disease. Acetone in human breath is the crucial biomarker for diabetes, which can be generated in the process of glucose metabolism and carbohydrate digestion.[39] Therefore, constructing high-performance acetone biomarkers sensor is considered a promising diagnostic tool for the early diagnosis of diabetes. Figure 5a shows a schematic illustration of the acetone sensing testing system. A broadband light is launched into the lead-in SMF from a light source. The sensing unit is hermetically fixed in a gas chamber. The transmission spectrum of the gas sensor is exported from the lead-out SMF and recorded by an optical spectrum analyzer. The transmission spectra of the HCF are measured in Figure 5b, and the

wavelength of the transmission spectra is red-shifted about 8 nm after the ZnO-Bi_2O_3 NSs is *in situ* grown on HCF due to the increased refractive index of the optical fiber surface.[16] ZnO-Bi_2O_3 NSs can effectively enhance the evanescent field of the surface, which is ultra-sensitive to local refractive index and thus more suitable for chemical gas detection. Experiments were conducted with the 3-cm-long HCF gas sensor exposed to the calibrated gas sample of acetone concentration in a pre-prepared chamber at room temperature. The acetone gas was pumped into the chamber with the stationary concentration, and the layer of ZnO-Bi_2O_3 NSs reacted with the target gas. The detailed experiments can be found in Supporting Information. Figure 5c shows the transmission spectrum as the acetone concentration changes from 0 ppm to 50 ppm, and the spectrum shifts towards the longer wavelength from 1540 nm to 1542.5 nm. The magnification is revealed that the red shift wavelength is about 2.5 nm (Figure 5d). The results indicated that the ZnO-Bi_2O_3 NSs have excellent adsorption with acetone molecules, which can be attributed to the electron transfer between the ZnO-Bi_2O_3 NSs and acetone molecules. The hole concentration decreases gradually with the process of electron transfer in the ZnO-Bi_2O_3 NSs, whereas the refractive index of ZnO-Bi_2O_3 NSs increases effectively.[40]

Figure 6a shows the wavelength shift as a function of time at room temperature during cyclic exposures of acetone for ZnO thin film gas sensor, and the corresponding shift values by plotting a line fitted curve from 10 ppm to 100 ppm is shown in Figure 6b. Compared to the ZnO thin film gas sensor (0.25 at 10 ppm), the ZnO-Bi_2O_3 NSs enabled HCF gas sensor (1.51 at 10 ppm) exhibits a 6-fold higher wavelength shift for acetone sensing, as shown in Figure 6c. Noted that the wavelength shift is negligible lower 10 ppm for the ZnO thin film gas sensor, while the ZnO-Bi_2O_3 NSs enabled HCF gas sensor shows outstanding wavelength shift in low ppm range due to the well-designed sheets morphology and ZnO-Bi_2O_3 heterojunction. Figure 6d shows two linear relationships between the wavelength shift and the acetone concentration for the ZnO-Bi_2O_3 NSs enabled HCF gas sensor. The wavelength shifts increase with the increasing of acetone concentration (the range is 0-100 ppm). In the low concentration range (0-10 ppm), a nonlinear fitting of the data follow relation $y = 0.017x - 0.002x^2 + 0.098$, where y is the wavelength shift, x is the acetone concentration. Meanwhile, the linear fitting of the data in the high concentration range is according to the equation $y = 0.929 + 0.033x$, the meaning of x and y are the same as above. The

results reveal that the HCF sensor is more sensitive in relatively low concentration, which can be attributed to the acetone molecules become saturated on the surface of ZnO-Bi_2O_3 NSs in the high concentration. Moreover, the theoretical limit of detection of the HCF sensor can be estimated with the formula $3SD/m$, where *SD* is the standard deviation of noise in the response curve, *m* is the slope of the linear part of the curve.[41] The calculation result is 140 ppb, which fulfills the requirement in the application of an exhaled breath sensor.[42] Figure 6e shows a complete cycle of gas adsorption and desorption for 1 ppm acetone on the surface of HCF, which causes saturation in the wavelength shift as a function of time and the data can be recorded in real-time by the spectrometer and computer. The wavelength signal increases sharply as the gas is pumped in, revealing fast gas adsorption kinetics, the corresponding response time lasts 25 s until the wavelength becomes unchanged and stable. Once exposed the HCF gas sensor into the air, the wavelength signal starts to recovery until back to the initial wavelength, and the recovery time is 44 s. The fast response and recovery times reveal that the process can keep in about one minute and provide the feasibility in the practical application. In addition, the selectivity is also one of the most important performance indicators for the HCF sensor. The wavelength shift to 1 ppm acetone is higher than that to 5 ppm other typical interfering gases (isopropanol, ethanol, methanol, formaldehyde) as shown in Figure 6f, which indicates the excellent acetone selectivity for the HCF sensor. This is owing to that the acetone (352 kJ mol^{-1}) bond dissociation energy is smaller than that of the isopropanol (380.7 kJ mol^{-1}), ethanol (462 kJ mol^{-1}), methanol (462 kJ mol^{-1}), formaldehyde (368 kJ mol^{-1}), which suggests that acetone is easier to react with the oxygen species on the surface of ZnO-Bi_2O_3 NSs than other interfering gases.[43-44] Repeatability and long-term stability are also important characteristics to evaluate the reliability of a sensor. Figure S7 shows the wavelength of transmission spectra can shift back to the original wavelength after the process of dynamical measurement and the wavelength shift has not changed between the two cycles. An additional long-term stability test is carried out for 1 ppm acetone, which can keep 80% of initial wavelength shift value over 60 days. The results reveal that the ZnO-Bi_2O_3 NSs in-situ grown in the HCF acetone sensor possess excellent repeatability and long-term stability. In addition, the **Table 1** shows the comparison between different sensing material-based optical fiber sensors for the acetone detection. As listed in the table, ZnO-Bi_2O_3 NSs enabled HCF gas sensor shows lower detection limit and higher sensitivity compared to other optical fiber sensors. All the above results indicate

that the ZnO-Bi_2O_3 NSs enabled HCF sensor exhibits excellent acetone sensing properties.

Table 1. Comparison between different sensing material-based optical fiber sensors for acetone detection.

Sensing materials	**Concentrations range of acetone**	**Detection limit**	**Sensitivity**	**References**
ZnO nanocrystalline	0-500 ppm	50 ppm	0.27/100 ppm	[45]
$Zn_3(VO_4)_2$ nanopowder	0-500 ppm	50 ppm	~0.15/100 ppm	[15]
$Ba_3 (VO_4)_2$ nanocrystalline	0-500 ppm	50 ppm	~0.1/100 ppm	[46]
$MnCo_2O_4$ nanoparticles	0-500 ppm	100 ppm	~0.2/100 ppm	[47]
$MgCo_2O_4$ nanosheets	0-500 ppm	100 ppm	0.081/500 ppm	[48]
Graphene	0-352 ppm	44 ppm	~0.4/352 ppm	[49]
γ-CuBr nanocrystals	0-750 ppm	50 ppm	~1.5/100 ppm	[50]
Mn–SnO_2 nanoparticles	0-500 ppm	50 ppm	~0.7/100 ppm	[51]
Nd doped mullite $Bi_2Fe_4O_9$	0-500 ppm	100 ppm	~1/100 ppm	[52]
ZnO-Bi_2O_3 NSs	0-100 ppm	140 ppb	4.5/100 ppm	This work

To further investigate the practical applications of the ZnO-Bi_2O_3 NSs enabled HCF sensor, the breath analysis is carried out towards healthy volunteers and simulated diabetes. It should be pointed out that the sensing performance is affected by humidity. To eliminate the effects of humidity, the exhaled breath sample is collected into a Tedlar bag (2L) through a self-made gas-drying device (Figure 7a and Figure S8) from 10 healthy volunteers consisting of 5 male and 5 female nonsmoking individuals. The device can effectively reduce the impact of high relative humidity (RH) from 90 RH% down to around 25 RH% in exhaled breath, which is full of cotton wool and silica gel.

Then, the collected samples are transferred into the gas chamber with 1.8 ppm acetone for the simulated breath of diabetic patients. In general, the acetone concentration in the diabetic exhaled breath is higher than 1.8 ppm, and lower than 0.9 ppm for healthy human.[53] Therefore, the simulated diabetic exhaled breath consists of a healthy volunteer breath and 1.8 ppm acetone. The transmission spectrum (Figure 7a) displayed an obvious redshift between the healthy volunteers and simulated diabetics, which is the ZnO-Bi_2O_3 NSs enabled HCF sensor has a highly sensitive and selective performance toward acetone in the exhaled breath background. Furthermore, Figure 7b also exhibits the ZnO-Bi_2O_3 NSs is *in situ* grown on HCF sensor can successfully discriminate the healthy breath and simulated diabetic breath through their spectrum shift values with a large difference of 3.5 times. Remarkably, the morphology of ZnO-Bi_2O_3 NSs (Figure S9) is largely preserved on the HCF after the exhaled breath measurements, which is critical for the long-term stability in the practical application. The above results demonstrate that the as-proposed HCF gas sensor has a high potential for early detection of diabetes.

Conclusion

In summary, the ZnO-Bi_2O_3 NSs heterostructure is grown *in situ* on the surface of HCF via the sol-gel and hydrothermal process for the first time. This technology presents a simple and novel route to coat micro-substrates with highly control and good morphological surface nanostructures. Combine with the change of the electron density for ZnO-Bi_2O_3 NSs and the refractive index of HCF, the wavelength shift can be recorded as the acetone pump into the test chamber. Therefore, the proposed sensor delivers a high-performance gas sensing to a large dynamic range (0-100 ppm) towards acetone at room temperature, especially in the less than 10 ppm concentration range. Meanwhile, it also demonstrated good repeatability, selectivity, long-term stability, with a satisfactory theoretical limit of detection (140 ppb), and a fast response and recovery cycle (response time is 25 s, recovery time is 44 s). A proof-of-concept experiment is performed on the exhaled breath from healthy volunteers and stimulated diabetic that can be successfully distinguish based on the wavelength shift signal, which provides a novel and convenient platform to design the gas sensor and pave a way for the early detection of diabetes.

Experimental Section

Preparation of ZnO seed layer in-situ grown in the HCF

ZnO seed layer was synthesized by a sol-gel method using PVP as a sacrificial template. First, the precursor solution for the ZnO seed layer was prepared. In a typical synthesis, 1.5 g PVP and 1.0 g $Zn(NO_3)_2$ was dissolved in 10 mL ethanol under moderate stirring for 30 min until the mixture formed a transparent solution. The as-prepared precursor solution was loaded into a capillary glass tube (0.9 mm diameter) with a seal at the bottom. Then, the as-prepared HCF was inserted into the capillary glass tube and drawn out slowly, this process was repeated three times in order to make sure the uniform of precursor on the HCF. Subsequently, the as-prepared sample was put into the drying oven for 30 min at 70 ℃. Finally, it was calcined at 350 ℃ under an air atmosphere for 3 h with a heating rate of 1 ℃ min^{-1} to remove the PVP template and product the ZnO seed layer.

Preparation of ZnO-Bi_2O_3 NSs in-situ grown in the HCF

First, the precursor solution for the ZnO-Bi_2O_3 NSs was prepared. 0.85 g of $Bi(NO_3)_3 \cdot 5H_2O$ was dissolved in 15 mL of ethylene glycol to completely obtain a transparent and uniform solution under moderate stirring for 30 min, and added 34 mL ethanol after that. The precursor solution was transferred into a Teflon-lined stainless steel autoclave. Then, the as-prepared HCF with ZnO seed layer was fixed vertically in the autoclave, and held for 1 h in order to ensure enough soaking. Then, the sample was put into a vacuum drying oven with the thermal treatment at 160 ℃ for 5 h. After the hydrothermal growth, the as-prepared HCF with ZnO seed layer was taken out, washed repeatedly with distilled water and ethanol to remove other residues and dried at 80 ℃ overnight in a vacuum.

Participants

Informed consent was obtained from participants who volunteered to perform these studies and this work is not following the scope of ethics approval.

Supporting Information

Supporting Information is available from the Wiley Online Library or from the author.

Acknowledgements

W.L. and Y.Z. contributed equally to this work. This work was supported by the

Singapore Ministry of Education Academic Research Fund Tier 2 (MOE2019-T2-2-127 and T2EP50120-0005), A*STAR under AME IRG (A2083c0062), the Singapore Ministry of Education Academic Research Fund Tier 1 (RG90/19 and RG73/19) and the Singapore National Research Foundation Competitive Research Program (NRF-CRP18-2017-02), Guangdong Basic and Applied Basic Research Foundation (2019A1515011762), Shenzhen Science and Technology Innovation Foundation (JCYJ20180305125302333, JCYJ20170818093035338, JCYJ20180305125430954), Shenzhen University Fund (860-000002110229) and Foshan City Education Department Foundation.

Conflict of Interest

The authors declare no conflict of interest.

Reference

[1] J. Shin, S.-J. Choi, I. Lee, D.-Y. Youn, C. O. Park, J.-H. Lee, H. L. Tuller, I.-D. Kim, *Adv. Funct. Mater.* **2013**, *23*, 2357.

[2] W. Liu, J. Sun, L. Xu, S. Zhu, X. Zhou, S. Yang, B. Dong, X. Bai, G. Lu, H. Song, *Nanoscale Horiz.* **2019**, *4*, 1361.

[3] G. Peng, U. Tisch, O. Adams, M. Hakim, N. Shehada, Y. Y. Broza, S. Billan, R. Abdah-Bortnyak, A. Kuten, H. Haick, *Nat. Nanotechnol.* **2009**, *4*, 669.

[4] Z. Wang, C. Hou, Q. De, F. Gu, D. Han, *ACS Sens.* **2018**, *3*, 468.

[5] I. Cho, Y. C. Sim, M. Cho, Y.-H. Cho, I. Park, *ACS Sens.* **2020**, *5*, 563.

[6] A. Paliwal, A. Sharma, M. Tomar, V. Gupta, *Sens. Actuators, B* **2017**, *250*, 679.

[7] C. Wongchoosuk, A. Wisitsoraat, A. Tuantranont, T. Kerdcharoen, *Sens. Actuators, B* **2010**, *147*, 392.

[8] G. Parmar, S. Lakhani, M. K. Chattopadhyay, presented at 2017 International Conference on Recent Innovations in Signal processing and Embedded Systems (RISE), 27-29 Oct. 2017, **2017**.

[9] S. Xu, H. Zhao, Y. Xu, R. Xu, Y. Lei, *ACS Appl. Mater. Interfaces* **2018**, *10*, 13895.

[10] C. Bariáin, I. R. Matías, I. Romeo, J. Garrido, M. Laguna, *Appl. Phys. Lett.* **2000**, *77*, 2274.

[11] H.-E. Joe, H. Yun, S.-H. Jo, M. B. G. Jun, B.-K. Min, *INT J PR ENG MAN-GT* **2018**, *5*, 173.

[12] J. Li, H. Yan, H. Dang, F. Meng, *Opt. Laser Technol.* **2021**, *135*, 106658.

[13] H. Fu, Q. Wang, J. Ding, Y. Zhu, M. Zhang, C. Yang, S. Wang, *Sens. Actuators, B* **2020**, *303*, 127186.

[14] N. A. M. Yahya, M. R. Y. Hamid, S. A. Ibrahim, B. H. Ong, N. A. Rahman, A. R. M. Zain, M. A. Mahdi, M. H. Yaacob, *Sens. Actuators, B* **2017**, *246*, 421.

[15] M. Subramanian, V. V. Dhayabaran, D. Sastikumar, M. Shanmugavadivel, *J. Alloys Compd.* **2018**, *750*, 153.

[16] H. Fu, Y. Jiang, J. Ding, J. Zhang, M. Zhang, Y. Zhu, H. Li, *Sens. Actuators, B* **2018**, *254*, 239.

[17] R. Forster, S. Weidlich, M. Nissen, T. Wieduwilt, J. Kobelke, A. M. Goldfain, T. K. Chiang, R. F. Garmann, V. N. Manoharan, Y. Lahini, M. A. Schmidt, *ACS Sens* **2020**, *5*, 879.

[18] C. Jain, A. Braun, J. Gargiulo, B. Jang, G. Li, H. Lehmann, S. A. Maier, M. A. Schmidt, *ACS Photonics* **2019**, *6*, 649.

[19] J. Zeng, Y. Li, X. Zheng, Z. Li, T. Zeng, W. Duan, Q. Li, X. Shang, B. Dong, *Anal. Chem.* **2019**, *91*, 5091.

[20] R. Rojaee, R. Shahbazian-Yassar, *ACS Nano* **2020**, *14*, 2628.

[21] S. P. Subin David, S. Veeralakshmi, J. Sandhya, S. Nehru, S. Kalaiselvam, *Sens. Actuators, B* **2020**, *320*, 128410.

[22] P. V. Shinde, B. G. Ghule, N. M. Shinde, Q. X. Xia, S. Shaikh, A. V. Sarode, R. S. Mane, K. H. Kim, *New J. Chem.* **2018**, *42*, 12530.

[23] Y. Huang, J. Guo, Y. Kang, Y. Ai, C. M. Li, *Nanoscale* **2015**, *7*, 19358.

[24] Z. Lai, Y. Chen, C. Tan, X. Zhang, H. Zhang, *Chem* **2016**, *1*, 59.

[25] X. Chen, S. Wang, C. Su, Y. Han, C. Zou, M. Zeng, N. Hu, Y. Su, Z. Zhou, Z. Yang, *Sens. Actuators, B* **2020**, *305*, 127393.

[26] Y. Kim, K. C. Kwon, S. Kang, C. Kim, T. H. Kim, S.-P. Hong, S. Y. Park, J. M. Suh, M.-J. Choi, S. Han, H. W. Jang, *ACS Sens.* **2019**, *4*, 2395.

[27] J. Ping, Z. Fan, M. Sindoro, Y. Ying, H. Zhang, *Adv. Funct. Mater.* **2017**, *27*, 1605817.

[28] P. Zhao, Y. Zhao, H. Bao, H. L. Ho, W. Jin, S. Fan, S. Gao, Y. Wang, P. Wang, *Nat. Commun.* **2020**, *11*, 847.

[29] J. Sun, C. C. Chan, *Sens. Actuators, B* **2007**, *128*, 46.

[30] M. Hou, F. Zhu, Y. Wang, Y. Wang, C. Liao, S. Liu, P. Lu, *Opt. Express* **2016**, *24*, 27890.

[31] S. Osbeck, R. H. Bradley, C. Liu, H. Idriss, S. Ward, *Carbon* **2011**, *49*, 4322.

[32] O. J. Ilegbusi, L. Trakhtenberg, *J. Mater. Eng. Perform.* **2013**, *22*, 911.

[33] V. Postica, J. Gröttrup, R. Adelung, O. Lupan, A. K. Mishra, N. H. de Leeuw, N. Ababii, J. F. C. Carreira, J. Rodrigues, N. B. Sedrine, M. R. Correia, T. Monteiro, V. Sontea, Y. K. Mishra, *Adv. Funct. Mater.* **2017**, *27*, 1604676.

[34] S. Liu, X. F. Lu, J. Xiao, X. Wang, X. W. Lou, *Angew. Chem., Int. Ed.* **2019**, *58*, 13828.

[35] W. Liu, X. Zhou, L. Xu, S. Zhu, S. Yang, X. Chen, B. Dong, X. Bai, G. Lu, H. Song, *Nanoscale* **2019**, *11*, 11496.

[36] H. Yuan, S. A. A. A. Aljneibi, J. Yuan, Y. Wang, H. Liu, J. Fang, C. Tang, X. Yan, H. Cai, Y. Gu, S. J. Pennycook, J. Tao, D. Zhao, *Adv. Mater.* **2019**, *31*, 1807161.

[37] L. Awin, B. J. Kennedy, M. Avdeev, *Ceram. Int.* **2013**, *39*, S233.

[38] M. Yakup Arıca, G. Bayramoğlu, M. Yılmaz, S. Bektaş, Ö. Genç, *J. Hazard. Mater.* **2004**, *109*, 191.

[39] M. Storer, J. Dummer, H. Lunt, J. Scotter, F. McCartin, J. Cook, M. Swanney, D. Kendall, F. Logan, M. Epton, *J. Breath Res.* **2011**, *5*, 046011.

[40] C. B. Yu, Y. Wu, X. L. Liu, B. C. Yao, F. Fu, Y. Gong, Y. J. Rao, Y. F. Chen, *Opt. Mater. Express* **2016**, *6*, 727.

[41] M. M. Alam, M. M. Rahman, M. T. Uddin, A. M. Asiri, Inamuddin, M. T. Saeed Chani, M. A. Islam, *J. Lumin.* **2020**, *227*, 117528.

[42] G. Konvalina, H. Haick, *Acc. Chem. Res.* **2014**, *47*, 66.

[43] S. Adhikari, X. Yang, Y. Xia, *Anal. Chem.* **2018**, *90*, 13036.

[44] W. Liu, Y. Xie, T. Chen, Q. Lu, S. Ur Rehman, L. Zhu, *Sens. Actuators, B* **2019**, *298*, 126871.

[45] B. Renganathan, A. R. Ganesan, *Opt. Fiber Technol.* **2014**, *20*, 48.

[46] M. Subramanian, V. Violet Dhayabaran, M. Shanmugavadivel, *Mater. Res. Bull.* **2019**, *119*, 110560.

[47] S. Vadivel, G. Balaji, S. Rathinavel, *Opt. Mater.* **2018**, *85*, 267.

[48] S. Rathinavel, S. Vadivel, G. Balaji, *Opt. Fiber Technol.* **2019**, *48*, 218.

[49] H. Zhang, A. Kulkarni, H. Kim, D. Woo, Y.-J. Kim, B. H. Hong, J.-B. Choi, T. Kim, *J. Nanosci. Nanotechnol.* **2011**, *11*, 5939.

[50] T. Subashini, B. Renganathan, A. Stephen, T. Prakash, *Mater. Sci. Semicond. Process.* **2018**, *88*, 181.

[51] P. Rajeshwaran, A. Sivarajan, *J. Mater. Sci.: Mater. Electron.* **2015**, *26,* 539.

[52] S. K. Rao, A. Kalai Priya, S. Manjunath Kamath, P. Karthick, B. Renganathan, S. Anuraj, D. Sastikumar, K. Jeyadheepan, C. Gopalakrishnan, *J. Alloys Compd.* **2020**, *838,* 155603.

[53] M. Righettoni, A. Tricoli, S. E. Pratsinis, *Anal. Chem.* **2010**, *82,* 3581.

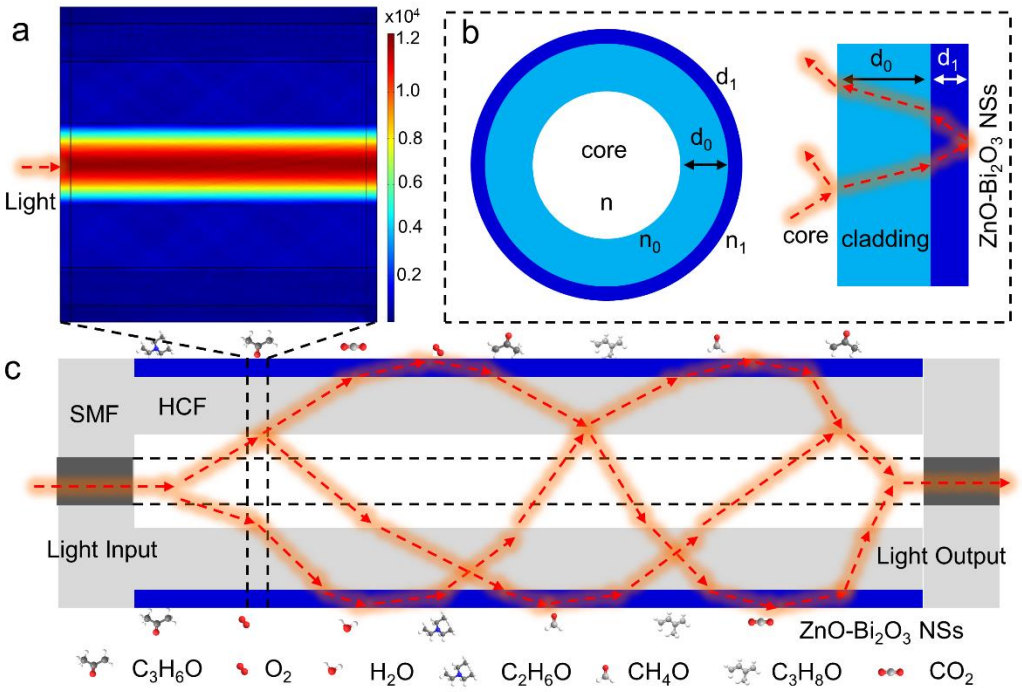

Figure 1. a) The mode field profile of HCF at the anti-resonant wavelength; b) Schematic diagram of the cross-section and profile of the HCF; c) A schema showing the SMF-HCF-SMF mode interferometer for the process of gas detection.

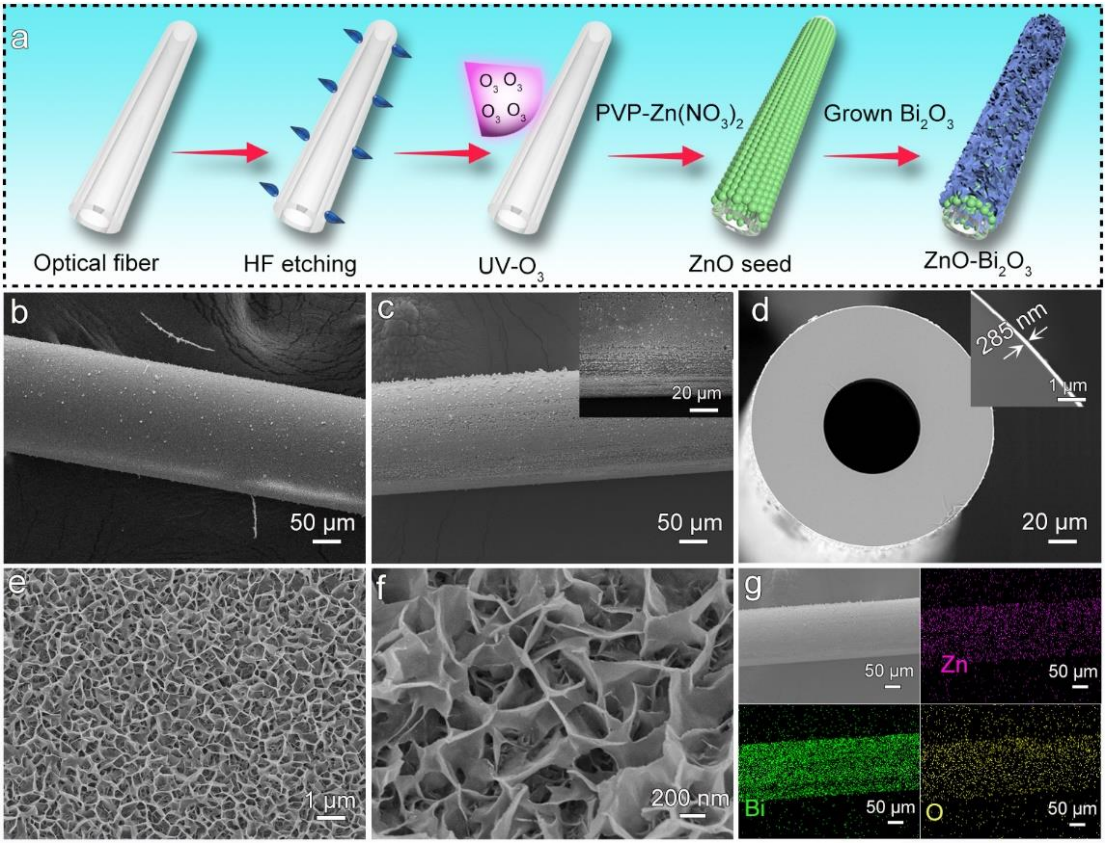

Figure 2. a) Illustration of the formation process of the ZnO-Bi_2O_3 NSs grown *in situ* on the HCF; b) FESEM image of the ZnO thin film grown on the HCF; c) FESEM image of the ZnO-Bi_2O_3 NSs grown on the HCF, the inset is the magnification with the larger scale; d) SEM cross-section image of the ZnO-Bi_2O_3 NSs grown on the HCF, the inset is the magnification with the larger scale; e, f) FESEM images of the surface of ZnO-Bi_2O_3 NSs with the different scales; g) the corresponding EDX mapping images of the ZnO-Bi_2O_3 NSs grown on the HCF.

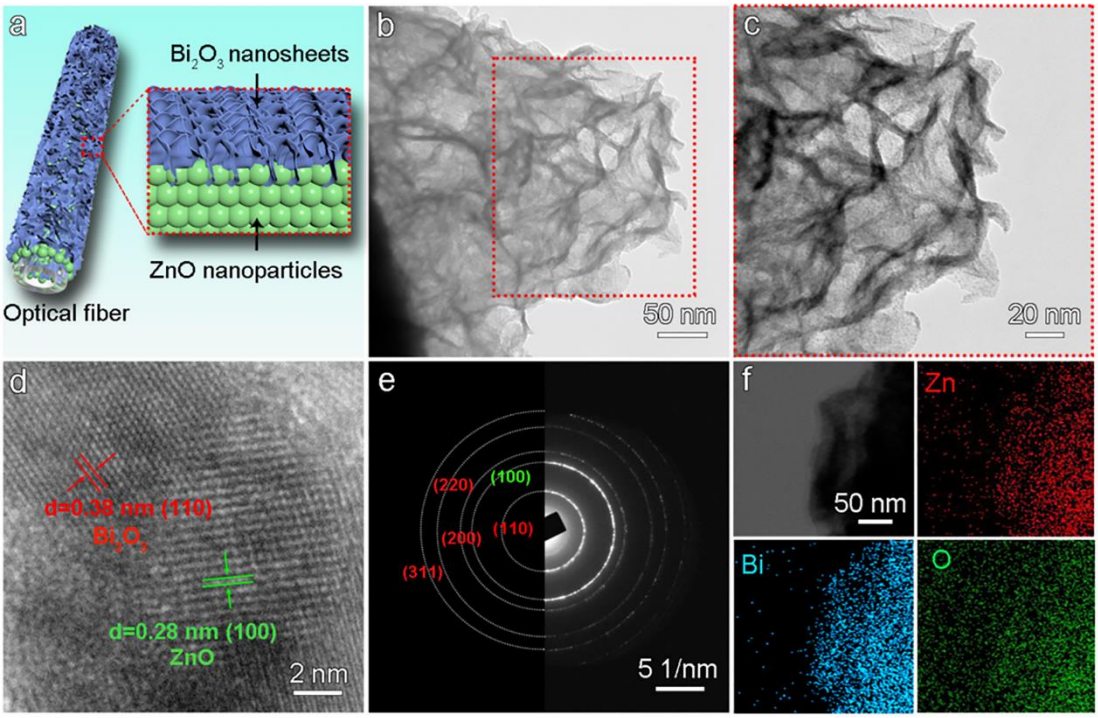

Figure 3. a) Diagram of the ZnO-Bi_2O_3 NSs grown on the HCF; b, c) TEM image of single ZnO-Bi_2O_3 NS with the different scales; d) HR-TEM image of the ZnO-Bi_2O_3 NS and (e) the corresponding SAED pattern and f) EDX mapping profiles.

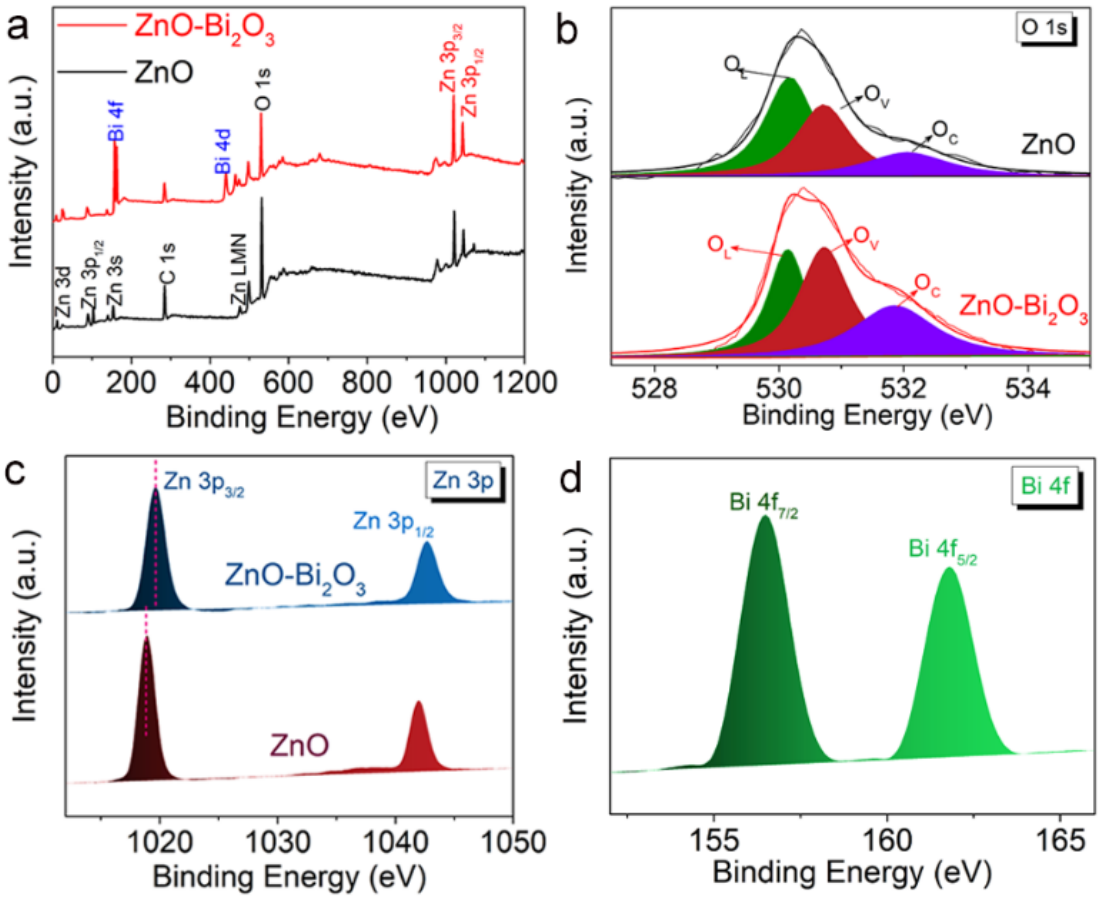

Figure 4. XPS survey of a) full-spectrum, b) O 1s, c) Zn 3p for ZnO thin film and ZnO-Bi_2O_3 NSs; XPS spectrum of d) Bi 4f for ZnO-Bi_2O_3 NSs.

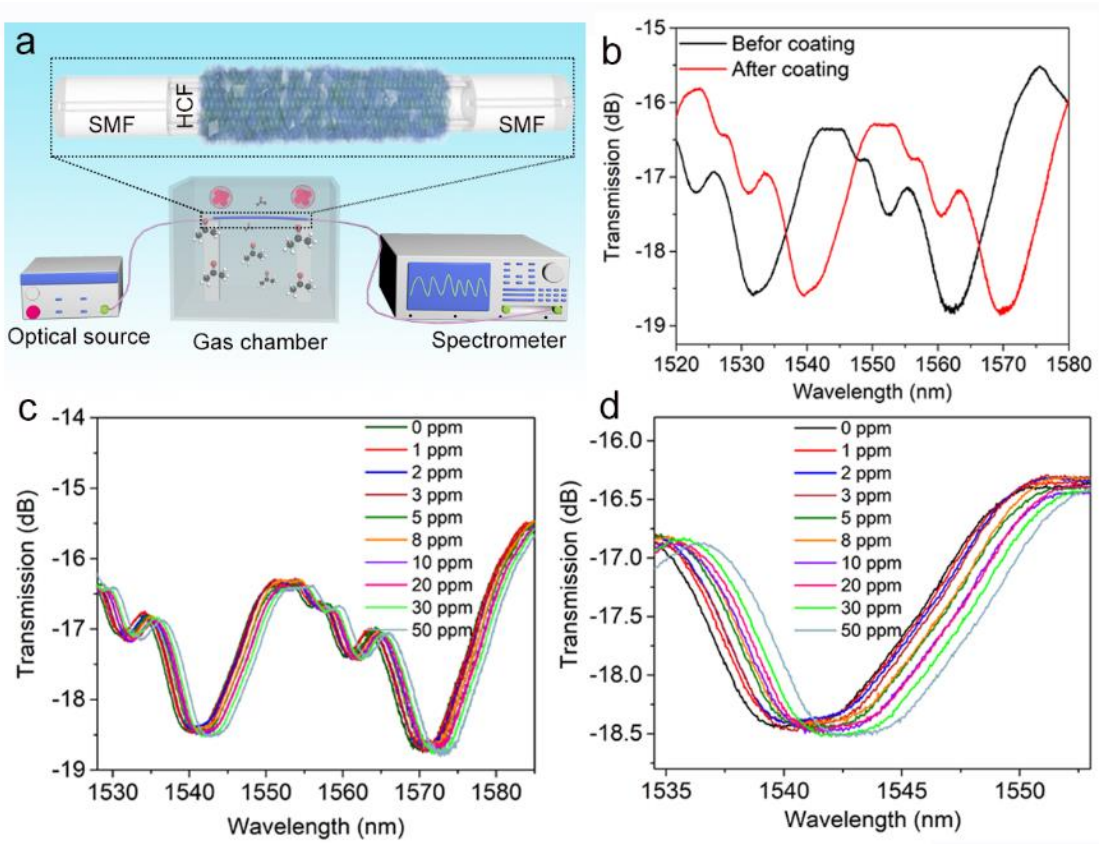

Figure 5. a) Schematic diagram of the experimental configuration; b) Transmission spectra of the HCF before and after in-situ grown ZnO-Bi_2O_3 NSs; c) Transmission spectra of the ZnO-Bi_2O_3 NSs in-situ grown on HCF gas sensor for the different acetone concentration; d) Enlarged spectra with the details of the wavelength redshift as the acetone concentration increases.

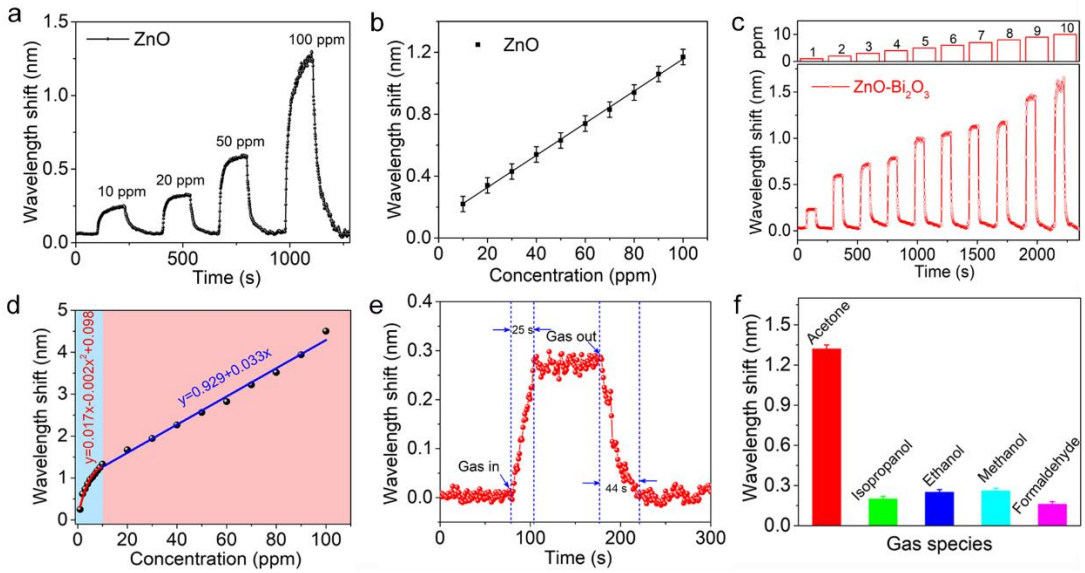

Figure 6. a) Dynamic curve and b) the corresponding linear relationship between the wavelength shift and various acetone concentration of ZnO thin film; c) Dynamic process of ZnO-Bi_2O_3 NSs in-situ grown on HCF gas sensor response to acetone from 1 ppm to 10 ppm at room temperature and d) the corresponding linear relationship between the wavelength shift and various acetone concentration; e) Response and recovery times for 1 ppm acetone in a complete adsorption and desorption cycle and f) the selectivity tests for the ZnO-Bi_2O_3 NSs in-situ grown on HCF gas sensor.

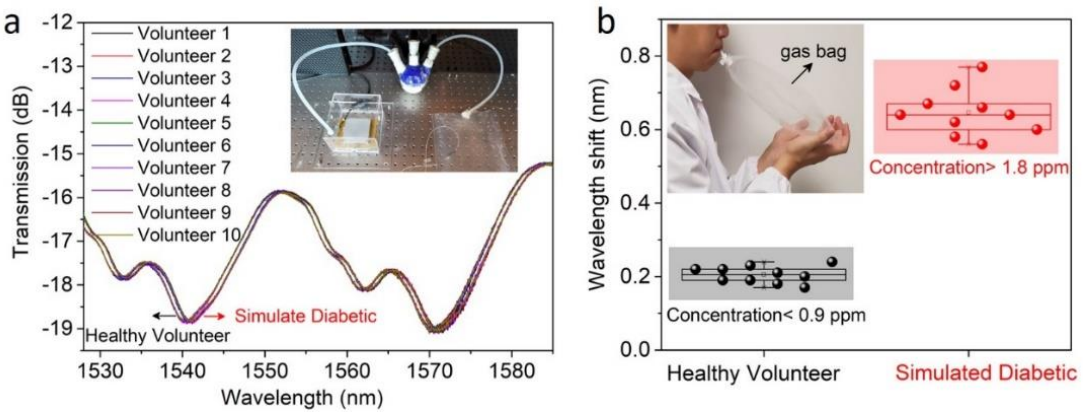

Figure 7. a) The transmission spectra of the ZnO-Bi_2O_3 NSs in-situ grown on HCF gas sensor for the detection of exhaled breath, the inset is the measurement system; b) Wavelength shift of HCF gas sensor from healthy volunteers and simulated diabetics breath, the inset is the collection process of exhaled breath.